DES16C3cje: A low-luminosity, long-lived supernova

C. P. Gutiérrez,[1]* M. Sullivan,[1] L. Martinez,[2,3] M. C. Bersten,[2,3,4] C. Inserra,[5] M. Smith,[1] J. P. Anderson,[6] Y.-C. Pan,[7] A. Pastorello,[8] L. Galbany,[9] P. Nugent,[10] C. R. Angus,[11] C. Barbarino,[12] T.-W. Chen,[13] T. M. Davis,[14] M. Della Valle,[15,16] R. J. Foley,[17] M. Fraser,[18] C. Frohmaier,[19] S. González-Gaitán,[20] G. F. Lewis,[21] M. Gromadzki,[22] E. Kankare,[23] R. Kokotanekova,[16] J. Kollmeier,[24] M. R. Magee,[25] K. Maguire,[25] A. Möller,[26] N. Morrell,[27] M. Nicholl,[28,29] M. Pursiainen,[1] J. Sollerman,[12] N. E. Sommer,[30] E. Swann,[19] B. E. Tucker,[30] P. Wiseman,[1] M. Aguena,[31,32] S. Allam,[33] S. Avila,[34] E. Bertin,[35,36] D. Brooks,[37] E. Buckley-Geer,[33] D. L. Burke,[38,39] A. Carnero Rosell,[40,32] M. Carrasco Kind,[41,42] J. Carretero,[43] M. Costanzi,[44,45] L. N. da Costa,[32,46] J. De Vicente,[40] S. Desai,[47] H. T. Diehl,[33] P. Doel,[37] T. F. Eifler,[48,49] B. Flaugher,[33] P. Fosalba,[50,51] J. Frieman,[33,52] J. García-Bellido,[34] D. W. Gerdes,[53,54] D. Gruen,[55,38,39] R. A. Gruendl,[41,42] J. Gschwend,[32,46] G. Gutierrez,[33] S. R. Hinton,[14] D. L. Hollowood,[17] K. Honscheid,[56,57] D. J. James,[58] K. Kuehn,[59,60] N. Kuropatkin,[33] O. Lahav,[37] M. Lima,[31,32] M. A. G. Maia,[32,46] M. March,[61] F. Menanteau,[41,42] R. Miquel,[62,43] E. Morganson,[42] A. Palmese,[33,52] F. Paz-Chinchón,[41,42] A. A. Plazas,[63] M. Sako,[61] E. Sanchez,[40] V. Scarpine,[33] M. Schubnell,[54] S. Serrano,[50,51] I. Sevilla-Noarbe,[40] M. Soares-Santos,[64] E. Suchyta,[65] M. E. C. Swanson,[42] G. Tarle,[54] D. Thomas,[19] T. N. Varga,[13,66] A. R. Walker,[67] R. Wilkinson[68]

(DES Collaboration)

Affiliations are listed at the end of the paper

ABSTRACT

We present DES16C3cje, a low-luminosity, long-lived type II supernova (SN II) at redshift 0.0618, detected by the Dark Energy Survey (DES). DES16C3cje is a unique SN. The spectra are characterized by extremely narrow photospheric lines corresponding to very low expansion velocities of $\lesssim 1500\,\mathrm{km\,s^{-1}}$, and the light curve shows an initial peak that fades after 50 days before slowly rebrightening over a further 100 days to reach an absolute brightness of $M_r \sim -15.5\,\mathrm{mag}$. The decline rate of the late-time light curve is then slower than that expected from the powering by radioactive decay of ^{56}Co, but is comparable to that expected from accretion power. Comparing the bolometric light curve with hydrodynamical models, we find that DES16C3cje can be explained by either i) a low explosion energy (0.11 foe) and relatively large ^{56}Ni production of $0.075\,\mathrm{M_\odot}$ from a $\sim 15\,\mathrm{M_\odot}$ red supergiant progenitor typical of other SNe II, or ii) a relatively compact $\sim 40\,\mathrm{M_\odot}$ star, explosion energy of 1 foe, and $0.08\,\mathrm{M_\odot}$ of ^{56}Ni. Both scenarios require additional energy input to explain the late-time light curve, which is consistent with fallback accretion at a rate of $\sim 0.5 \times 10^{-8}\,\mathrm{M_\odot\,s^{-1}}$.

Key words: supernovae: general — supernovae: individual (DES16C3cje)

1 INTRODUCTION

Recent wide-field sky surveys have revealed a significant diversity in the observed properties of supernovae (SNe).

These events have covered a wide range of observed characteristics: transients with extremely bright luminosities (e.g., superluminous SNe, Gal-Yam 2012); transients with a rapid temporal evolution spanning a range of luminosities (e.g., Perets et al. 2010; Kasliwal et al. 2012; Drout et al. 2014; Pursiainen et al. 2018), and a heterogeneous population of

---

* E-mail: C.P.Gutierrez-Avendano@soton.ac.uk

transients with a slow temporal evolution (e.g., Taddia et al. 2016; Arcavi et al. 2017; Terreran et al. 2017). These new SN discoveries have in turn created new challenges for the SN field, particularly concerning the SN progenitor and the physics of the explosion.

In the canonical picture of a core-collapse SN, the explosion releases $\sim 10^{51}$ erg of energy (1 foe), and a fraction of the progenitor's material is burned into various intermediate-mass and iron-peak elements. The early emission from SNe ($\leqslant 5$ days after explosion) is powered by the release of shock deposited energy, while the power source from the peak to late-phases is provided by the decay of ^{56}Ni into ^{56}Co and subsequently ^{56}Fe. In slow- and fast-declining hydrogen-rich SNe (historical SNe IIP and SNe IIL, respectively), the plateau is producing by the recombination mechanisms. However, some core-collapse SNe have larger explosion energies, which typically require an additional source of energy to explain the luminosity and evolution (see review, and references therein, of Moriya et al. 2018a). Pair-Instability SNe (PISNe; e.g. Heger & Woosley 2002; Gal-Yam et al. 2009), magnetars (e.g. Kasen & Bildsten 2010), accretion power (e.g. Moriya et al. 2010; Dexter & Kasen 2013), and pulsational pair-instability (PPI; e.g. Woosley et al. 2007; Woosley 2017) have all been proposed as a source of additional energy, but as yet there is no clear consensus about the relative importance of each source nor associations to specific transients.

Recently, two peculiar type II SNe (SNe II) have been studied in detail: iPTF14hls (Arcavi et al. 2017) and OGLE-2014-SN-073 (Terreran et al. 2017). iPTF14hls is a SN with very little spectral evolution over ~ 600 days, and with a light curve that shows multiple re-brightening events. OGLE-2014-SN-073 is a very bright SN with an unusually broad light curve, combined with high ejecta velocities in its spectra. Both objects exploded in low-luminosity galaxies and require an extra source of power (beyond shock energy and radioactivity) to explain their unusual evolution.

One of the most studied scenarios to explain the peculiar behaviour of these two transients is the fallback accretion. Moriya et al. (2018b) found that fallback accretion can reproduce the shape of the light curve, luminosity and photospheric velocities of OGLE-2014-SN-073, while Arcavi et al. (2017) and Wang et al. (2018) proposed that iPTF14hls may be powered by intermittent fallback accretion. The idea of fallback in SNe was introduced by Colgate (1971), and has been broadly studied to determine its effects on the central remnant (e.g. Chevalier 1989; Woosley & Weaver 1995; Fryer 1999), and on SN light curves (e.g. Fryer et al. 2009; Moriya et al. 2010; Dexter & Kasen 2013). Dexter & Kasen (2013) showed that the accretion power may be relevant to explain peculiar and rare SNe.

In this paper, we present the photometry and spectra of DES16C3cje, an unusual SN II discovered by the Dark Energy Survey Supernova Program (DES-SN; Bernstein et al. 2012). We discuss its peculiar characteristics and examine the late-time light curve under the fallback scenario. In Section 2 we describe our observations of DES16C3cje and measurements. We analyse the spectral and photometric properties and compare them with other similar events in Section 3, and then discuss the progenitor scenarios that could explain the event in Section 4. We discuss and conclude in Section 5.

Throughout, we assume a flat ΛCDM universe, with a Hubble constant of $H_0 = 70 \,\mathrm{km\,s^{-1}\,Mpc^{-1}}$, and $\Omega_\mathrm{m} = 0.3$.

2 OBSERVATIONS

DES16C3cje was detected by DES using the wide-field Dark Energy Camera (DECam; Flaugher et al. 2015) instrument in an r-band image taken on 2016 October 11 (JD = 2457673.3) with an apparent magnitude of $r = 23.26$ mag. The transient was located at $\alpha = 03^\mathrm{h}28^\mathrm{m}35\overset{\mathrm{s}}{.}29$, $\delta = -27°09'06\overset{\prime\prime}{.}6$ (J2000.0) in a faint host galaxy ($M_r \sim -18.5$ mag) at a redshift of 0.0616. The previous non-detection with DES was obtained on 2016 October 7 (MJD = 57667.6), with a detection limit of $z \sim 25.1$ mag. This limit places a constraint on the explosion epoch of ± 2.6 days; we adopt 2016 October 9 (the intermediate epoch; MJD = 57670.2 ± 2.6 d) as the explosion date. Further information on the DES-SN difference-imaging search pipeline and machine-learning algorithms to identify transient objects can be found in Kessler et al. (2015) and Goldstein et al. (2015).

Photometric coverage of DES16C3cje was acquired by DES-SN in *griz* filters from 2016 October until 2017 February, and then from 2017 August to 2018 February. Between 2017 February and 2017 July, additional photometric data were obtained by the extended Public European Southern Observatory (ESO) Spectroscopic Survey for Transient Objects (ePESSTO; Smartt et al. 2015) and other collaborators with the ESO Faint Object Spectrograph and Camera 2 (EFOSC2; Buzzoni et al. 1984) at the 3.6m ESO New Technology Telescope (NTT), with the FOcal Reducer/low dispersion Spectrograph 2 (FORS2; Appenzeller et al. 1998) at the ESO Very Large Telescope (VLT), with the Low Dispersion Survey Spectrograph 3 (LDSS3; Osip et al. 2004) on the Magellan Clay 6.5-m telescope, and with the the Gamma-Ray Burst Optical/Near-Infrared Detector (GROND; Greiner et al. 2008), at the 2.2-m MPG telescope at the European Southern Observatory (ESO) La Silla Observatory.

The NTT data were reduced using the PESSTO pipeline (Smartt et al. 2015), while for the FORS2 images we used the ESOREFLEX pipeline (Freudling et al. 2013). Reductions for data obtained with LDSS3 were performed with Image Reduction and Analysis Facility (IRAF; Tody 1986) using standard routines. Images from the MPG were reduced with the GROND pipeline (Krühler et al. 2008). The DES photometric measurements were made using the pipeline discussed by Papadopoulos et al. (2015) and Smith et al. (2016), which has also been extensively used in the literature (e.g., Firth et al. 2015, and references therein). This pipeline subtracts a deep template image from each individual DES image to remove the host-galaxy light using a point-spread-function (PSF) matching routine. SN photometry is then measured from the difference image using a PSF-fitting technique. The photometry of DES16C3cje is reported in Appendix A1.

DES16C3cje was observed spectroscopically on six epochs from +47 to +403 days (throughout the paper, we give all epochs relative to the explosion epoch). These observations were obtained with four different instruments: The AAOmega spectrograph at the Anglo-Australian Telescope (AAT), X-SHOOTER (Vernet et al. 2011) and FORS2 at

the VLT, and Gemini Multi-Object Spectrograph (GMOS-S; Hook et al. 2004) at the Gemini Observatory. A log of the spectroscopic observations of DES16C3cje is reported in Table 1. Spectroscopic reductions for X-SHOOTER were performed using the ESOREFLEX pipeline, FORS2 data were reduced with IRAF using standard routines, while for GMOS-S we used the Gemini IRAF package, combined with IDL routines to flux calibrate the data and remove telluric lines.

3 CHARACTERIZING DES16C3CJE

3.1 Host galaxy properties

The host galaxy of DES16C3cje was identified as PGC3243310, a low-luminosity galaxy (M_B^{host} = −18.26 ± 0.50 mag[1]) at a redshift of 0.0618[2]. Adopting the recessional velocity corrected into the CMB frame[3] (v= 18465 ± 89 km s^{-1}), we obtain a distance of 275.95 Mpc, which corresponds to μ = 37.20. The galactic reddening in the direction of PGC3243310 is $E(B - V)$ = 0.17 mag (Schlafly & Finkbeiner 2011). Due to the faintness of the galaxy and the absence of the absorption Na I D lines in the SN spectra, we assume the host extinction negligible.

Using a spectrum obtained by OzDES with the AAOmega at the AAT (see Sec. 3.4) and a spectrum from the 2dF Galaxy Redshift Survey (Colless et al. 2003), we estimate the integrated oxygen abundance. The lack of [N II] suggests a very low metallicity. Setting the upper limits of the flux ratio of Hα/[[N II]λ6583 and measuring the ratio of [O III]λ5007/Hβ, we estimate the upper limit of the metallicity. Applying the O3N2 diagnostic method from Marino et al. (2013), we obtain an oxygen abundance of 12 + log(O/H) < 8.19 ± 0.02. With the luminosity of Hα and the equation of Kennicutt & Evans (2012), we calculate the SFR to be 0.042 M$_\odot$ yr^{-1}.

3.2 Light curves

The unusual photometric evolution of DES16C3cje from ∼ +2 to +450 days is presented in Figure 1 (top panel). The light curves show an initial increase in brightness for the first 20 days followed by a decrease, particularly in the bluer filters, as observed in some SNe II (e.g., SN 2004em, SN 2004ek; Taddia et al. 2016). In the redder bands, the luminosity increase monotonically, with a change in the slope at ∼ 60 days. After 60 days, the g-band increases ∼ 1.4 mag over 70 days versus ∼ 1.0 mag in *riz*.

We use Gaussian processes (GPs) to interpolate the observed light curves (see de Jaeger et al. 2017; Inserra et al. 2018b; Angus et al. 2019, for more details). The interpolation was performed with the Python package GEORGE (Ambikasaran et al. 2016) using the Matern 3/2 kernel. We find that DES16C3cje reaches a peak brightness of ∼ −15.75 ± 0.10 mag at 152 ± 5 days in the *r*-band. The long rise is reminiscent of SN 1987A, but over a longer scale; this behavior has not previously been observed in a SN II light curve. During the later phases (after ∼ 300 days), the light curves show a linear decline in *riz* and a flat evolution in the *g*-band. The slope of the decline in the *r*-band light curve is 0.70 mag per 100 days, smaller than that expected from the full trapping of gamma-ray photons and positrons from the decay of ^{56}Co (0.98 mag per 100 days; Woosley et al. 1989).

In the middle panel of Figure 1, the colour curves are presented. During the first 65 days (in the bump), DES16C3cje becomes redder, changing from $g - r$ = 0.37 to $g - r$ = 0.85. The SN then evolves to bluer colours. At late-phases (> +300 days), the object has a redder colour than during the first two months, but its evolution is relatively flat.

3.3 Bolometric luminosity and Nickel mass

Using the *griz* photometric data, we compute the pseudo-bolometric and bolometric light curves for DES16C3cje (Figure 1, bottom panel) following the prescriptions presented by Inserra et al. (2018a). Here, the *griz* bands are converted into fluxes at the effective filter wavelengths, and then corrected for the Milky Way extinction. A spectral energy distribution (SED) is then computed over the wavelengths covered and the flux under the SED is integrated assuming zero flux beyond the integration limits. Fluxes are converted to luminosities using the adopted distance (275.95 Mpc). We determined the points on the pseudo-bolometric light curves at epochs when *griz* were available simultaneously. Magnitudes from the missing bands were generally estimated by interpolating or extrapolating the light curves using low-order polynomials (n≤3) and assuming constant colours from nearest epochs. Therefore, we obtain a peak luminosity of L_{bol} = (4.96 ± 0.10) × 10^{41} erg s^{-1}, and L_{griz} = (2.33 ± 0.08) × 10^{41} erg s^{-1}.

As expected based on the photometric data, the bolometric light curves decline slowly at late phases. This decline rate is slower than the radioactive decay of ^{56}Co, but comparable to that expected from accretion power. Although the light curve tail does not follow the ^{56}Co decay, we can still use the luminosity at late times to estimate an upper limit to the ^{56}Ni mass. Comparing the bolometric light curve of DES16C3cje to that of SN 1987A, we estimate the ^{56}Ni mass, $M(^{56}$Ni$)_{16cje}$, as follows:

$$M(^{56}\text{Ni})_{16cje} \approx M(^{56}\text{Ni})_{87A} \times \frac{L_{16cje}}{L_{87A}} \, M_\odot, \qquad (1)$$

where $M(^{56}$Ni$)_{87A}$ = 0.075 ± 0.005 M$_\odot$ is the ^{56}Ni mass synthesised by SN 1987A (Arnett 1996) and L_{87A} is the bolometric luminosity at a comparable epoch. This comparison gives $M(^{56}$Ni$)_{16cje}$ ≈ 0.068 M$_\odot$, a comparatively large value for typical SN II, but within the range of SN 1987A-like objects (Müller et al. 2017; Anderson 2019).

3.4 Spectral evolution

In Fig. 2, we present the optical spectra obtained for DES16C3cje between +47 d and +380 d. At 47 d, the spectrum is completely dominated by the emission lines from the host galaxy, with no traces of the SN. From 80 d, the spectra show that DES16C3cje is a SN II with very narrow photospheric lines. At 80 d and 127 d, DES16C3cje presents

---

[1] http://leda.univ-lyon1.fr/

[2] Redshift obtained from the narrow emission lines of the host galaxy

[3] http://ned.ipac.caltech.edu/

Table 1. Spectroscopic observations of DES16C3cje.

UT date	MJD (days)	Rest-frame phase[★] (days)	Telescope + Instrument	Range (Å)	Grism/Grating/ Arm
20161127	57719.7	47	AAT+AAOmega	$3750 - 9000$	580V+385R
20170102	57755.6	80	Gemini+GMOS-S	$5700 - 7500$	R400-G5305
20170129	57782.0	105	VLT+XSHOOTER	$3100 - 10400$	UV/VIS/NIR
20170221	57805.0	127	VLT+XSHOOTER	$3100 - 10400$	UV/VIS/NIR
20170731	57965.3	278	VLT+FORS2	$4300 - 9500$	300V+GG435
20171116	58074.2	380	VLT+XSHOOTER	$3600 - 9600$	UV/VIS/NIR

[★] The phase is relative to the estimated explosion date, MJD= 57670.2 ± 2.6 d.

characteristic P-Cygni profiles of Hα, Hβ, Fe II λ4924, Fe II λ5018, Fe II λ5169, Na I D λ5893 and the Ca II near-IR triplet, together with a lack of Sc II and Ba II lines. The 'Cachito' feature, related to high velocity (HV) spectra components (Gutiérrez et al. 2017), are also visible at these epochs, suggesting an interaction between the SN ejecta and circumstellar material (CSM). The later spectra are dominated by Hα, with a weak contribution of the Ca II near-IR triplet in emission. There is no evidence of forbidden lines (e.g., [O I] $\lambda\lambda$6300, 6363, [Fe II] λ7155 and [Ca II] λ7291, 7323), which are typical of core-collapse SNe at late phases. The lack of these lines could suggest either a high density associated with a large mass and low-velocity or an interaction between the SN ejecta and the CSM (Sec. 5).

DES16C3cje shows a complex Hα P-cygni profile (Figure 2, right panel). At early times (spectra between 80 d and 127 d), the absorption component increases in strength with time, from 3.8 ± 0.5 Å to 8.5 ± 1.2 Å; however, at 278 d and 380 d, this component is absent. The emission component at earlier times shows a Gaussian profile with an extra narrow emission line, caused by a contaminating H II region. At late times, the Hα emission has a Lorentzian profile with a FWHM velocity of 815 ± 65 km s^{-1} at 295 d, increasing to 980 ± 55 km s^{-1} at 403 d. The absence of the absorption component, and the Lorentzian profile in emission, further indicate interaction between the ejecta and the CSM (Chugai et al. 2004). At 380 d, on the top of the emission component of the Hα, a small notch is observed; upon close examination this was revealed to be residuals from the galaxy subtraction[4].

Based on the width of the lines observed in the SN spectra, we infer very low expansion velocities. The velocity obtained for Hα decreases from ~ 1500 km s^{-1} at 80 d, to ~ 1300 km s^{-1} at 127 d. The velocities found for other lines show a similar behavior: low expansion velocities (< 2000 km s^{-1}), and little evolution.

3.5 Comparison to other supernovae

The slow rise of DES16C3cje is reminiscent of SN 1987A-like objects, whereas its low luminosity and low expansion velocities are a common characteristic in low luminosity (LL) SNe II. In Figure 3, we show the photometric and spectral

comparison of DES16C3cje with these two classes of events. For the SN 1987A-like objects we compared with SN 1987A (Bouchet et al. 1989; Hamuy & Suntzeff 1990), which is the best observed and studied SN II; SN 2004ek (Taddia et al. 2016) and SN 2004em (Taddia et al. 2016), which both show a bump before the main peak; SN 2005ci (Taddia et al. 2016) and SN 2009E (Pastorello et al. 2012), which are the faintest clones of SN 1987A. For the LL SNe II, we select objects with spectra at around 110 days: SN 1999br (Pastorello et al. 2004; Galbany et al. 2016; Gutiérrez et al. 2017), which is the faintest slowly-declining SN II; SN2003Z (Spiro et al. 2014; Faran et al. 2014), SN 2005cs (Pastorello et al. 2006, 2009), and SN 2013K (Tomasella et al. 2018), which all have good photometric coverage in the first 150 days. The long rise to peak is common between the SN1987A-like events and DES16C3cje; however, the rise is even longer for DES16C3cje.

The full light curve evolution shows that DES16C3cje, from explosion to 60 d, exhibits a initial 'bump'. Although this bump is not common in SN1987A-like objects, two other SNe do show it: SN 2004ek and SN 2004em (Taddia et al. 2016). Taddia et al. (2016) suggest that these two SNe are an intermediate case between SN 1987A and normal SNe II. Pastorello et al. (2012) argue that these bumps are due to shock cooling. DES16C3cje also has the lowest luminosity within the SN1987A-like group, around 1 mag fainter than SN 1987A and ~ 0.5 mag fainter than the low-luminosity SN 2009E.

Comparing to the LL-SNe II sample, the initial evolution of DES16C3cje is consistent with typical SNe II for ~ 60 d; however a sudden increase in luminosity transforms a 'typical SN II' to a SN1987A-like event. The post-peak light curve evolution also differs, where all SN1987A-like and LL-SNe follow the rate of ^{56}Co decay. In the case of DES16C3cje, the decay at late-times is slower; again suggesting an extra source of energy is needed. To distinguish between the scenarios of ^{56}Co decay and accretion power ($L \propto t^{-5/3}$) as explanations for the light curves, we compare the chi-squared (χ^2) values (shown in Table A2) of the corresponding fits to the SNe with data at late-time (DES16C3cje, SN 1987A, SN 2005cs and SN 2009E). Out of these, only for DES16C3cje does the power law provides a better fit, supporting the theory of an extra source of energy. Because of the large uncertainties in the bolometric light curve of DES16C3cje, we test this result using a Monte Carlo resampling with 10^5 random draws (assuming a Gaus-

---

[4] The expansion velocities and the pseudo-equivalent-widths were measured removing the contribution of the host galaxy.
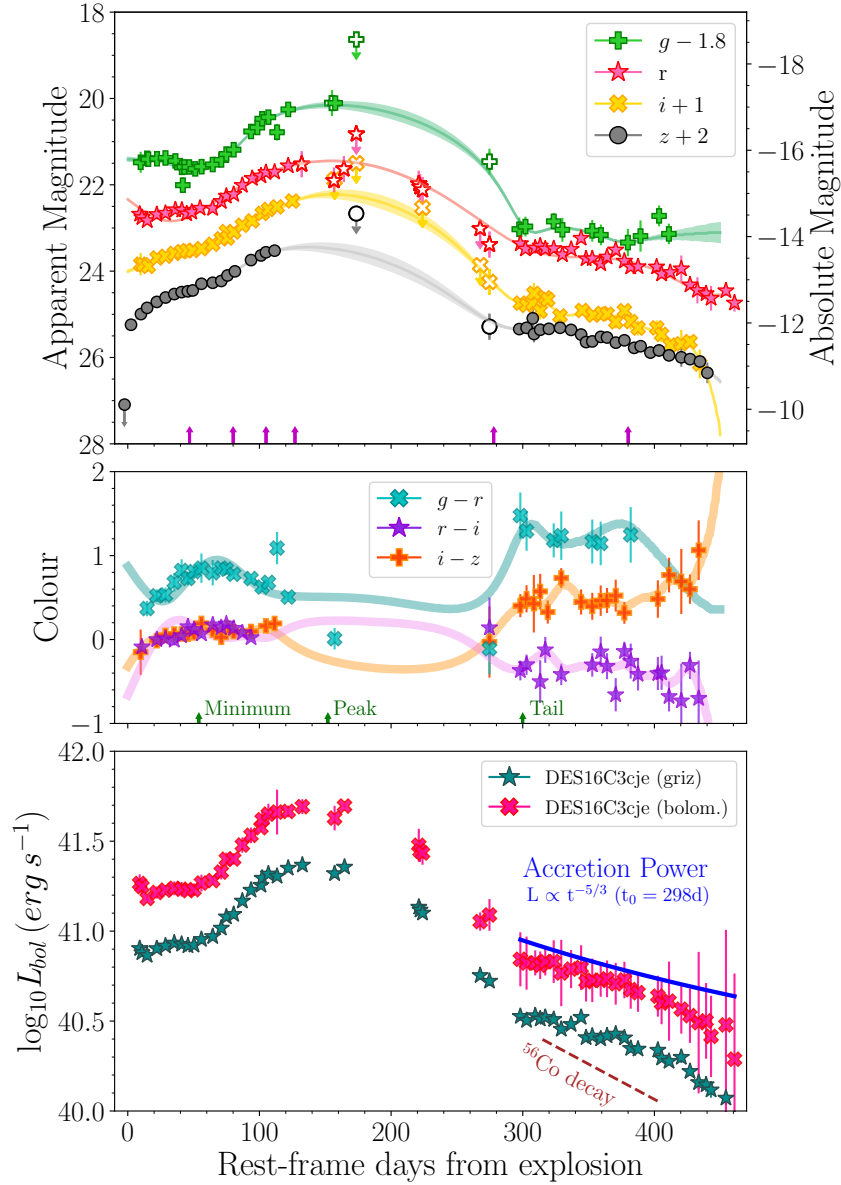
**Figure 1. Upper:** *griz* light curves of DES16C3cje. Filled symbols represent the data obtained with DES, while open stars show the data obtained with EFOSC2, LDSS3, FORS2 and GROND. Only corrections for Milky Way extinction have been made. The last non-detection is presented as a green arrow. Vertical purple arrows represent epochs of optical spectroscopy. Solid lines show the Gaussian process (GP) interpolation. **Middle:** Colour curves of DES16C3cje. Solid lines show the GP interpolation. Vertical green arrows represent epochs of minimum, peak and the beginning of the tail in the optical light curves. **Lower:** Bolometric (pink) and pseudo-bolometric (dark cyan) light curves of DES16C3cje. The dashed line shows the luminosity expected from ^{56}Co (assuming full trapping) and the solid line the luminosity expected from accretion power.

sian distribution). The results obtained support our previous findings.

Figure 3 also presents the spectral comparison at ∼ 105 d from explosion. The comparison with SN1987A-like objects and LL-SNe II again shows that DES16C3cje is a unique object. None of the other SNe have lines as narrow as DES16C3cje. SN 1999br has the narrowest lines, but its spectrum also shows Ba II and Sc II, together with a multiple component Hα P-Cygni profile, characteristic of LL-SNe II.

4 LIGHT CURVE MODELLING

We now consider some models that can be used to understand and explain the physical origin and unusual features of DES16C3cje. For these models, we use the one-dimensional Lagrangian hydrodynamical code presented in Bersten et al. (2011). This code simulates a SN explosion, and produces bolometric light curves and photospheric velocities to characterize the progenitor and explosion properties. There are two particular challenges to this modelling: the early-time to peak photometric and spectral velocities, and the late-time decline rate. We begin with the former.
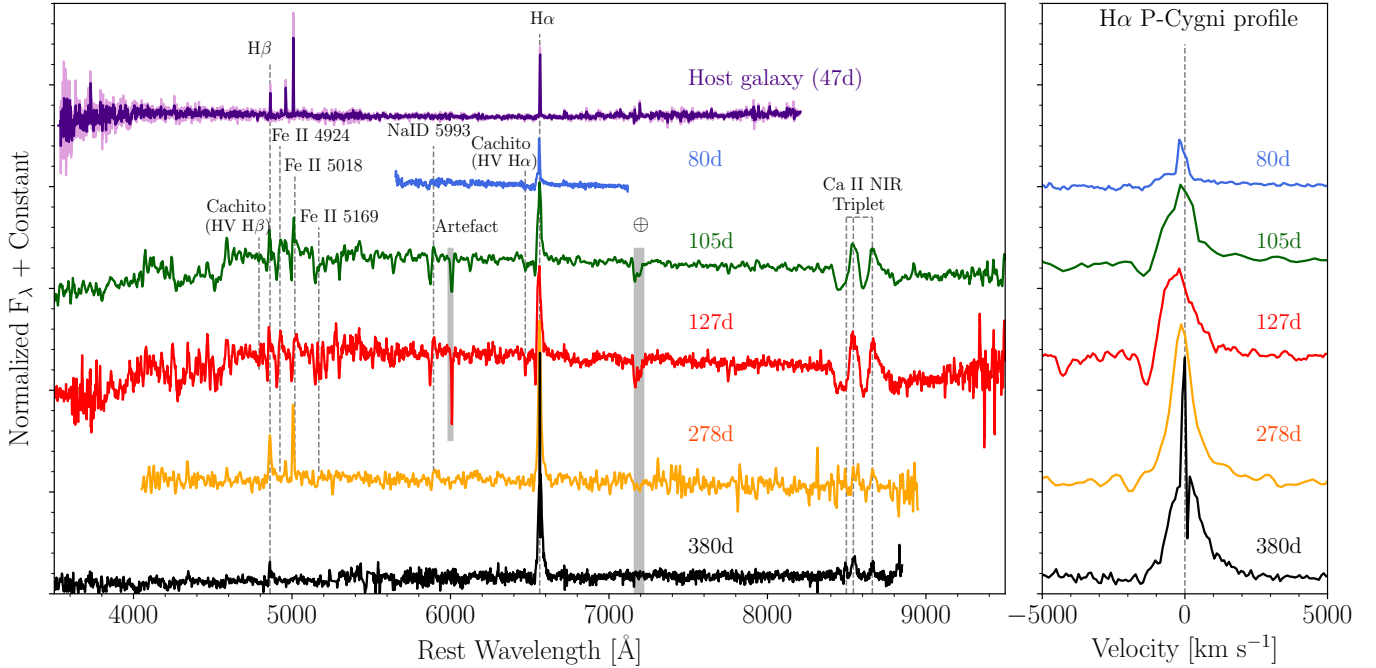
Figure 2. Left: Optical spectra of DES16C3cje from 80 to 380 days after explosion. Each spectrum has been corrected for Milky Way reddening and shifted by an arbitrary amount for presentation. The phases are labelled on the right. **Right:** Zoom around the Hα P-Cygni profile in velocity space.

There is a degree of degeneracy between the progenitor (pre-SN) mass and radius (M, R) and the explosion energy (E), which can be partially reduced by modeling the luminosity evolution together with the expansion velocity evolution. For DES16C3cje, the expansion velocities imply a low E/M ratio. This means that for a progenitor with similar characteristics to those used for SN 1987A (i.e., a blue supergiant star with $R \sim 50\,R_\odot$, $M_{ZAMS} = 20\,M_\odot$ and $E = 1$ foe), there is no model that simultaneously matches the light curve and velocity evolution, as a low energy is needed to reproduce the latter. This low energy leads to a much fainter and broader light curve than that observed. We found that explosion energies of ~ 0.1 foe are needed to reproduce the expansion velocities of DES16C3cje.

Therefore, we calculated a grid of hydrodynamical models with values of E close to 0.1 foe. Our pre-SN models were computed using the stellar evolution code MESA version 10398 (Paxton et al. 2011, 2013, 2015, 2018). The stars were evolved from the pre-main-sequence to the time of core collapse, defined as when any part of the collapsing core exceeds an infall velocity of $1000\,km\,s^{-1}$, and assuming solar metallicity. After exploring several configurations (see Figure B.1 in the Appendix), we found a model that reproduced relatively well the observations. This model is presented on the left panel of Figure 4 and has the following physical parameters: a $M_{ZAMS} = 15\,M_\odot$, a pre-SN mass of $13.3\,M_\odot$, $R = 830\,R_\odot$ and $E = 0.11$ foe. A relatively large ^{56}Ni mass of $0.095\,M_\odot$ was required to reproduce the light curve observed after the initial bump. This material was mixed up to 0.75 of the pre-SN mass, and therefore a not too extreme mixing was required as is common in several 87A-like objects. In this scenario, the peculiar light curve shape of DES16C3cje can

be understood as a combination of a low explosion energy and a relatively large ^{56}Ni production, while its progenitor has a red supergiant (RSG) structure typical of other SN II objects.

We now turn to the late-time light curve. Despite the good agreement between the model and observations at early times, there are clear differences in the slopes during the light curve tail (green curve in Figure 4). As discussed above, DES16C3cje does not follow the behavior expected by radioactive decay of ^{56}Co, but instead is consistent with a power law $\propto t^{-5/3}$, compatible with the decline rate expected from accretion power (or 'fallback' [5]; Michel 1988; Chevalier 1989). Under some conditions, for example if the SN explosion is not powerful enough, some material may not acquire sufficient energy to escape and will eventually be accreted onto the compact remnant. These accretions are usually associated with powerful energy outflows. A fraction of this energy can be thermalised within the SN ejecta and thus power the light curve (Dexter & Kasen 2013).

We have included this extra energy in our 1D Lagrangian code to explore if this can improve the differences between the model and observations during the latter part of the light curve. The rate input of energy due to the accretion can be written as: $L_{fb} = \dot{E} = \eta\,\dot{M}\,c^2$ where $\dot{M}$ is the fallback accretion rate, c is the speed of light and η is the

---

[5] The canonical power-law index, $n = -5/3$, is produced by a simple ballistic fallback model (Rees 1988). However, standard viscous disc descriptions extend the duration of the emission, with an index closer to $n = -1.2$ (see Balbus & Mummery 2018, and references therein). This suggests that the index value n changes depending on the conditions of the disc.
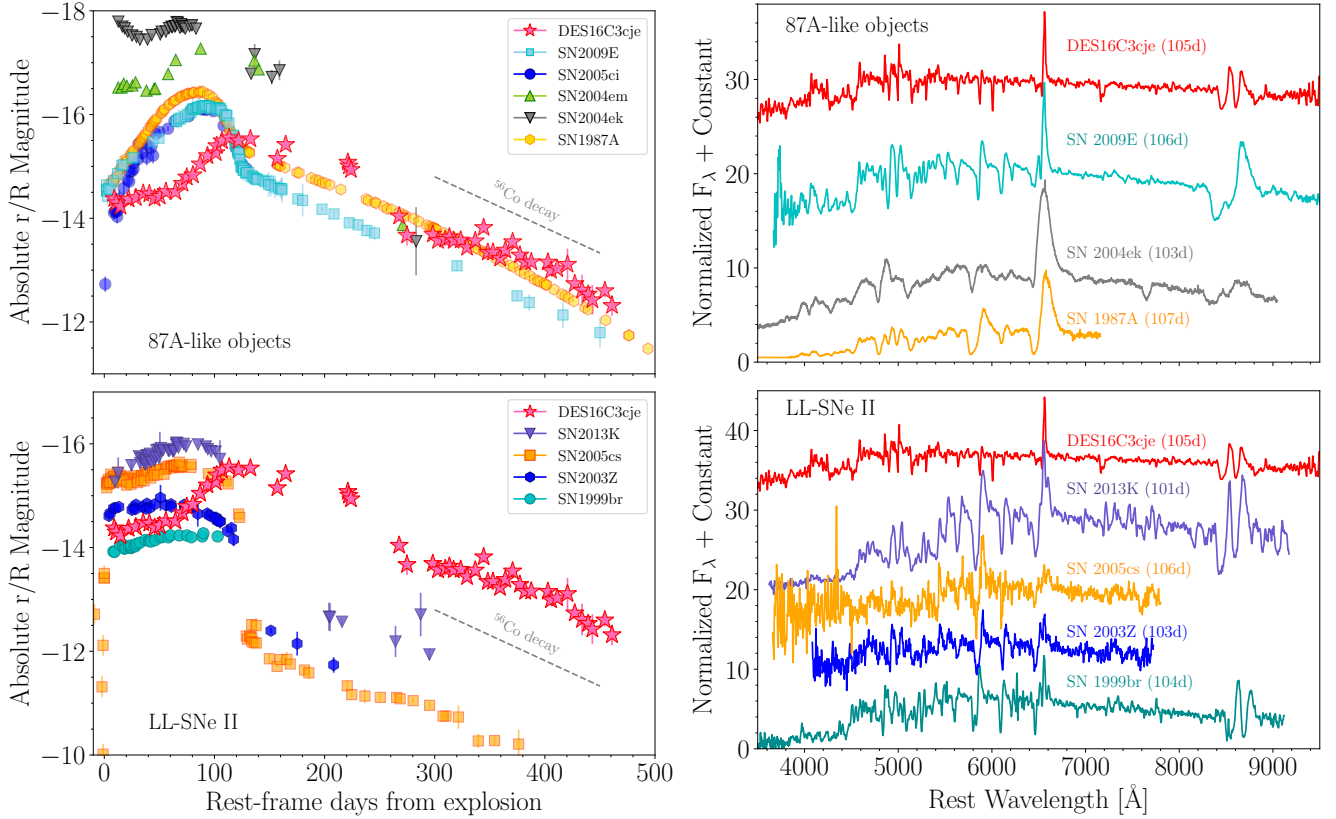
Figure 3. Left: Comparison of the r/R-band light curve of DES16C3cje with well-observed SNe II. Upper panel: Comparison with 87A-like objects: SN 1987A (Bouchet et al. 1989; Hamuy & Suntzeff 1990), SN 2004ek (Taddia et al. 2016), SN 2004em (Taddia et al. 2016), SN 2005ci (Taddia et al. 2016) and SN 2009E (Pastorello et al. 2012). Lower panel: Comparison with LLSNe II: SN 1999br (Pastorello et al. 2004; Galbany et al. 2016), SN2003Z (Spiro et al. 2014; Faran et al. 2014), SN 2005cs (Pastorello et al. 2009), and SN 2013K (Tomasella et al. 2018). Right: Spectral comparison around 110 d for DES16C3cje. Upper panel: Comparison with SN1987A-like objects: SN 1987A (Phillips et al. 1988), SN 2004ek (Taddia et al. 2016), and SN 2009E (Pastorello et al. 2012). Lower panel: Comparison with LLSNe II: SN 1999br (Gutiérrez et al. 2017), SN2003Z (Spiro et al. 2014), SN 2005cs (Pastorello et al. 2009), and SN 2013K (Tomasella et al. 2018).

efficiency factor, estimated to be of the order of 10^{-3} (Dexter & Kasen 2013). Analytic estimates (Chevalier 1989), as well as numerical simulations (Zhang et al. 2008; Dexter & Kasen 2013), have shown that the accretion rate can be assumed to be $\dot{M} = \dot{M}_0(t/t_0)^{-5/3}$, where $\dot{M}_0$ is the accretion rate onto the remnant at a time t_0 when the fallback episode begins. The fallback energy is deposited near the center of the progenitor, and we assume full trapping.

In our treatment, $\dot{M}_0$ and t_0 are free parameters to be determined by comparison with the observations. We again calculate a grid of simulations for different values of $\dot{M}_0$ and t_0, finding a set of parameters that can reproduce the behaviour of the light curve tail of DES16C3cje. The fallback parameters found are: $\dot{M}_0 = 0.5 \times 10^{-8}\,M_\odot\,\mathrm{s}^{-1}$ and $t_0 = 1\,\mathrm{d}$. These calculations were performed assuming the same progenitor and explosion energy as the RSG model presented above, and the combined model is shown in Figure 4. The inclusion of fallback energy clearly improves the modelling during the tail, with almost no effect in other phases. However, we note a slightly smaller amount of ^{56}Ni is needed when fallback energy is added; a good match is found using $0.075\,M_\odot$ of ^{56}Ni. The value of $\dot{M}_0$ is small compared with that usually found in the literature (Zhang et al. 2008;

Moriya et al. 2018a). The reason is the low luminosity of this SN: larger accretion rates inject more energy and produce brighter light curves.

The parameters of our preferred model point to a normal RSG progenitor that has experienced a low energy explosion leading to the fallback process. The peculiar light curve shape of DES16C3cje can then be explained as a combination of a low explosion energy, a relatively large and mixed ^{56}Ni production, and extra energy due to the accretion of material onto the compact remnant.

There is strong evidence of the existence of a correlation between the explosion energy and the amount of ^{56}Ni (see for example Pejcha & Prieto 2015), in the sense that more energetic events produce larger amount of ^{56}Ni. This relation is also supported by theoretical studies. The low explosion energy and the relatively large ^{56}Ni production found in our modelling does not follow the expected correlation. We note a low explosion energy was also required to reproduce the photospheric velocities.

DES16C3cje has only two measurements of the expansion velocity available at ~ 105 d and ~ 127 d, and thus the expansion velocity during the first weeks of evolution is not unambiguously known, and the measurements around
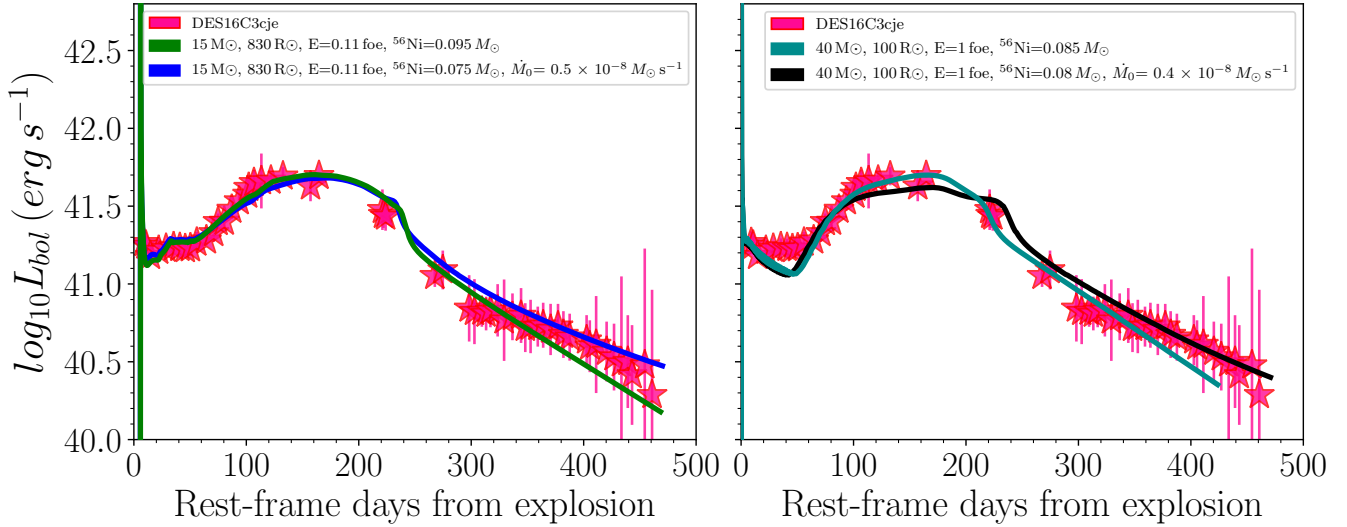
Figure 4. Bolometric light curve of DES16C3cje (stars) compared with the results of the light curve calculations from hydrodynamic models (Section 4). A core-collapse explosion (powered only by ^{56}Ni) is presented in green on the left panel and in cyan on the right. Explosions powered by both ^{56}Ni and fallback (i.e., with an extra contribution of energy coming from accretion in the central region) are presented in blue and black in each panel. The parameters used for each model are given in the legends.

~ 100 d may not represent the photospheric velocities of the ejecta. We experiment with relaxing the condition to reproduce the expansion velocity, and find an alternative model that reproduces relatively well the observed light curve with a progenitor with ~40 M$_\odot$, an explosion energy of 1 foe and 0.08 M$_\odot$ of ^{56}Ni (Figure 4). Here, we used a polytropic model to describe the structure of the star before explosion. The fallback parameters needed to reproduce the tail are similar to that in the previous model, i.e, $\dot{M}_0 = 0.4 \times 10^{-8}$ M$_\odot$ s^{-1} and $t_0 = 1$ d. The higher energy of this model is then consistent with known correlations between ^{56}Ni production and explosion energy. Figure B.2 shows the different configurations explored for this case. The parameters of the best-fit models are presented in Table A3.

5   DISCUSSION AND CONCLUSIONS

DES16C3cje is a low-luminosity and low-velocity type II supernova (SN II). Its light curves show a bump for ~ 60 days, followed by a long rise time, reminiscent of SN 1987A, but on a longer time-scale. The initial faint bump is due to hydrogen recombination, while the broad peak is powered by radioactive decay. After 300 days, the tail presents a decline rate comparable to that expected from accretion power ($\propto t^{-5/3}$). The narrow lines observed in the spectra imply low expansion velocities, and thus, low explosion energies. Taken together, these characteristics suggest an unusual explosion.

Modelling the light curve of DES16C3cje and its velocity evolution with hydrodynamical calculations, we have shown that the SN is consistent with the explosion of a RSG star with a mass of 15 M$_\odot$, an energy of 0.11 foe, and synthesising a ^{56}Ni mass of 0.075 M$_\odot$. Because of the low energy in the explosion, some material is accreted by the compact remnant with an accretion rate of ~ 0.5 × 10^{-8} M$\odot$ s^{-1}. Although this scenario reproduces the light curve and veloci-

ties, at first sight the required ^{56}Ni mass appears relatively large for two main reasons: 1) low energy explosions are observed to produce small amounts of ^{56}Ni, and 2) in the fallback scenario, some amount of the ^{56}Ni is expected to be accreted on to the central remnant.

However, Chevalier (1989) discussed the expectation that an ejection of substantial ^{56}Ni would imply little mass fallback, and showed this is not valid for accretion after the passage of the reverse shock wave, when the ^{56}Ni is expected to mix with outer core layers. Heger & Woosley (2010) further showed that a considerable amount of ^{56}Ni comes out when mixing precedes fallback. The mixing in RSGs is larger than in compact objects as perturbations have more time to grow before freezing out. Under these considerations, it is not unusual to find SNe that both experienced some fallback and have a relatively large amount of ^{56}Ni.

Nonetheless, we also consider an alternative scenario by assuming that the velocities measured from the absorption lines at 105 and 126 days do not represent the photospheric velocities of the ejecta. We then find that DES16C3cje can be modelled as the explosion of a relatively compact star ($R = 100$ R$_\odot$), with a mass of ~ 40 M$_\odot$, an explosion energy of 1 foe, and a ^{56}Ni mass of 0.08 M$_\odot$.

Both models can reproduce the overall evolution of the light curve of DES16C3cje; however, the low-energy explosion of a RSG fits the early part of the light curve better, and provides a good agreement with expansion velocities.

A further possibility to explain the late-time light curve of DES16C3cje is interaction with CSM. Interacting objects (e.g. SNe IIn, SN 2009ip-like objects; Stritzinger et al. 2012; Fraser et al. 2015; Elias-Rosa et al. 2016; Pastorello et al. 2018) often have flattened late-time light curves, with decline rates slower than that expected for ^{56}Co decay. The flat evolution in the light curves of DES16C3cje, together with the lack of [O II] $\lambda\lambda$6300, 6363, [Fe II] λ7155 and [Ca II] λ7291, 7323 emission lines, offer some support for this sce-

nario. However, this evidence for interaction only appears at around 300 days from explosion with no evidence for interaction prior to this epoch, in turn suggesting a significant mass loss during the progenitor star evolution.

Theoretical models have also shown that stars with masses below 40 $M_\odot$ at low-metallicities undergo very little mass loss due to stellar winds (e.g. Woosley et al. 2007; Meynet et al. 2013). Assuming that the progenitor mass favored by our hydrodynamical models (15 and 40$M_\odot$) is correct, we would expect a low mass loss. The location of our object supports this argument: DES16C3cje exploded in a low-luminosity (low-metallicity, Sec. 3.1) host, and models predict low-metallicity stars have less mass loss and bigger hydrogen envelopes when they explode (e.g. Heger et al. 2003).

While the late-time light curve of DES16C3cje is following a decline rate close to $t^{-5/3}$, we cannot rule out a scenario involving interaction with CSM. Moriya et al. (2019) briefly discuss the possibility of CSM interaction in fallback SN and the need to study this issue in the future.

In summary, we have shown that the fallback SN scenario can naturally explain the slow decline in the late-time light curve. However, further investigations are needed to interpret the origin of these peculiar objects, the signatures required to identify the explosion scenario, and the role of the ^{56}Ni mass and interaction with CSM.

REFERENCES

Ambikasaran S., et al., 2016, IEEE Trans. Pattern Anal. Mach. Intell., 38
Anderson J. P., 2019, A&A, 628, A7
Angus C. R., et al., 2019, MNRAS, p. 1302
Appenzeller I., et al., 1998, The Messenger, 94, 1
Arcavi I., et al., 2017, Nature, 551, 210
Arnett D., 1996, Supernovae and Nucleosynthesis: An Investigation of the History of Matter from the Big Bang to the Present
Balbus S. A., Mummery A., 2018, MNRAS, 481, 3348
Bernstein J. P., et al., 2012, ApJ, 753, 152
Bersten M. C., Benvenuto O., Hamuy M., 2011, ApJ, 729, 61
Bouchet P., Moneti A., Slezak E., Le Bertre T., Manfroid J., 1989, A&AS, 80, 379
Buzzoni B., et al., 1984, The Messenger, 38, 9
Chevalier R. A., 1989, ApJ, 346, 847
Chugai N. N., et al., 2004, MNRAS, 352, 1213
Colgate S. A., 1971, ApJ, 163, 221
Colless M., et al., 2003, VizieR Online Data Catalog, p. VII/226
Dexter J., Kasen D., 2013, ApJ, 772, 30
Drout M. R., et al., 2014, ApJ, 794, 23
Elias-Rosa N., et al., 2016, MNRAS, 463, 3894
Faran T., et al., 2014, MNRAS, 442, 844
Firth R. E., et al., 2015, MNRAS, 446, 3895
Flaugher B., et al., 2015, AJ, 150, 150
Fraser M., et al., 2015, MNRAS, 453, 3886
Freudling W., Romaniello M., Bramich D. M., Ballester P., Forchì V., García-Dabló C. E., Moehler S., Neeser M. J., 2013, A&A, 559, A96
Fryer C. L., 1999, ApJ, 522, 413
Fryer C. L., et al., 2009, ApJ, 707, 193
Gal-Yam A., 2012, Science, 337, 927
Gal-Yam A., et al., 2009, Nature, 462, 624
Galbany L., et al., 2016, AJ, 151, 33
Goldstein D. A., et al., 2015, AJ, 150, 82
Greiner J., et al., 2008, PASP, 120, 405
Gutiérrez C. P., et al., 2017, ApJ, 850, 89
Hamuy M., Suntzeff N. B., 1990, AJ, 99, 1146
Heger A., Woosley S. E., 2002, ApJ, 567, 532
Heger A., Woosley S. E., 2010, ApJ, 724, 341
Heger A., Fryer C. L., Woosley S. E., Langer N., Hartmann D. H., 2003, ApJ, 591, 288
Hook I. M., Jørgensen I., Allington-Smith J. R., Davies R. L., Metcalfe N., Murowinski R. G., Crampton D., 2004, PASP, 116, 425
Inserra C., et al., 2018a, MNRAS, 475, 1046
Inserra C., Prajs S., Gutierrez C. P., Angus C., Smith M., Sullivan M., 2018b, ApJ, 854, 175
Kasen D., Bildsten L., 2010, ApJ, 717, 245
Kasliwal M. M., et al., 2012, ApJ, 755, 161
Kennicutt R. C., Evans N. J., 2012, ARA&A, 50, 531
Kessler R., et al., 2015, AJ, 150, 172

Krühler T., et al., 2008, ApJ, 685, 376
Marino R. A., et al., 2013, A&A, 559, A114
Meynet G., Eggenberger P., Ekström S., Georgy C., Groh J., Maeder A., Saio H., Moriya T., 2013, in Alecian G., Lebreton Y., Richard O., Vauclair G., eds, EAS Publications Series Vol. 63, EAS Publications Series. pp 373–383 (arXiv:1308.5797), doi:10.1051/eas/1363042
Michel F. C., 1988, Nature, 333, 644
Moriya T., Tominaga N., Tanaka M., Nomoto K., Sauer D. N., Mazzali P. A., Maeda K., Suzuki T., 2010, ApJ, 719, 1445
Moriya T. J., Sorokina E. I., Chevalier R. A., 2018a, Space Sci. Rev., 214, 59
Moriya T. J., Terreran G., Blinnikov S. I., 2018b, MNRAS, 475, L11
Moriya T. J., Müller B., Chan C., Heger A., Blinnikov S. I., 2019, ApJ, 880, 21
Müller T., Prieto J. L., Pejcha O., Clocchiatti A., 2017, ApJ, 841, 127
Osip D. J., et al., 2004, in Moorwood A. F. M., Iye M., eds, Society of Photo-Optical Instrumentation Engineers (SPIE) Conference Series Vol. 5492, Proc. SPIE. pp 49–59, doi:10.1117/12.552414
Papadopoulos A., et al., 2015, MNRAS, 449, 1215
Pastorello A., et al., 2004, MNRAS, 347, 74
Pastorello A., et al., 2006, MNRAS, 370, 1752
Pastorello A., et al., 2009, MNRAS, 394, 2266
Pastorello A., et al., 2012, A&A, 537, A141
Pastorello A., et al., 2018, MNRAS, 474, 197
Paxton B., Bildsten L., Dotter A., Herwig F., Lesaffre P., Timmes F., 2011, The Astrophysical Journal Supplement Series, 192, 3
Paxton B., et al., 2013, The Astrophysical Journal Supplement Series, 208, 4
Paxton B., et al., 2015, ApJS, 220, 15
Paxton B., et al., 2018, ApJS, 234, 34
Pejcha O., Prieto J. L., 2015, ApJ, 799, 215
Perets H. B., et al., 2010, Nature, 465, 322
Phillips M. M., Heathcote S. R., Hamuy M., Navarrete M., 1988, AJ, 95, 1087
Pursiainen M., et al., 2018, preprint, (arXiv:1803.04869)
Rees M. J., 1988, Nature, 333, 523
Schlafly E. F., Finkbeiner D. P., 2011, ApJ, 737, 103
Smartt S. J., et al., 2015, A&A, 579, A40
Smith M., et al., 2016, ApJ, 818, L8
Spiro S., et al., 2014, MNRAS, 439, 2873
Stritzinger M., et al., 2012, ApJ, 756, 173
Taddia F., et al., 2016, A&A, 588, A5
Terreran G., et al., 2017, Nature Astronomy, 1, 713
Tody D., 1986, in Crawford D. L., ed., Society of Photo-Optical Instrumentation Engineers (SPIE) Conference Series Vol. 627, Instrumentation in astronomy VI. p. 733, doi:10.1117/12.968154
Tomasella L., et al., 2018, MNRAS, 475, 1937
Vernet J., et al., 2011, A&A, 536, A105
Wang L. J., et al., 2018, ApJ, 865, 95
Woosley S. E., 2017, ApJ, 836, 244
Woosley S. E., Weaver T. A., 1995, ApJS, 101, 181
Woosley S. E., Pinto P. A., Hartmann D., 1989, ApJ, 346, 395
Woosley S. E., Blinnikov S., Heger A., 2007, Nature, 450, 390
Zhang W., Woosley S. E., Heger A., 2008, ApJ, 679, 639
de Jaeger T., et al., 2017, MNRAS, 472, 4233

APPENDIX A: TABLES

Table A1. Photometry of DES16C3cje

UT date p	MJD	Rest-frame phase (days)	*g* (mag)	*r* (mag)	*i* (mag)	*z* (mag)	Instrument
20161011	57673.3	2.9	–	–	–	23.26 ± 0.08	DECam
20161018	57680.3	9.5	–	22.71 ± 0.13	–	–	DECam
20161019	57681.1	10.3	23.31 ± 0.24	–	22.86 ± 0.26	23.01 ± 0.08	DECam
20161020	57682.1	11.2	–	22.78 ± 0.06	22.87 ± 0.05	–	DECam
20161024	57686.3	15.2	23.22 ± 0.08	22.85 ± 0.05	–	22.86 ± 0.08	DECam
20161025	57687.2	16.0	23.24 ± 0.08	–	22.91 ± 0.07	–	DECam
20161101	57694.1	22.5	23.23 ± 0.07	22.71 ± 0.03	22.71 ± 0.06	22.73 ± 0.06	DECam
20161108	57701.1	29.1	23.21 ± 0.08	22.68 ± 0.03	22.67 ± 0.03	22.62 ± 0.03	DECam
20161115	57708.2	35.8	23.28 ± 0.10	22.60 ± 0.04	22.61 ± 0.05	22.54 ± 0.05	DECam
20161121	57714.1	41.3	23.43 ± 0.13	22.61 ± 0.05	22.57 ± 0.04	22.50 ± 0.04	DECam
20161122	57715.1	42.3	23.84 ± 0.18	–	–	–	DECam
20161123	57716.2	43.3	23.42 ± 0.09	–	–	–	DECam
20161126	57719.2	46.1	23.42 ± 0.08	22.70 ± 0.03	22.54 ± 0.03	22.48 ± 0.03	DECam
20161201	57724.1	50.8	23.47 ± 0.08	22.66 ± 0.03	22.54 ± 0.05	22.46 ± 0.04	DECam
20161207	57730.1	56.4	23.42 ± 0.17	22.57 ± 0.03	22.50 ± 0.04	22.31 ± 0.04	DECam
20161216	57739.2	65.0	23.37 ± 0.15	22.57 ± 0.03	22.40 ± 0.03	22.28 ± 0.04	DECam
20161223	57746.1	71.5	23.26 ± 0.04	22.41 ± 0.02	22.27 ± 0.02	22.24 ± 0.02	DECam
20161227	57750.2	75.3	23.12 ± 0.06	22.29 ± 0.03	22.10 ± 0.04	–	DECam
20161228	57751.1	76.2	–	–	22.25 ± 0.03	22.11 ± 0.03	DECam
20170102	57756.1	80.9	23.02 ± 0.06	22.25 ± 0.02	22.11 ± 0.02	22.02 ± 0.03	DECam
20170109	57763.1	87.5	–	22.04 ± 0.03	21.96 ± 0.02	–	DECam
20170116	57770.1	94.1	22.60 ± 0.03	21.88 ± 0.01	21.85 ± 0.01	21.76 ± 0.02	DECam
20170121	57775.2	98.9	22.51 ± 0.04	–	–	–	DECam
20170124	57778.1	101.6	–	21.82 ± 0.02	–	21.65 ± 0.02	DECam
20170125	57779.1	102.6	22.31 ± 0.04	21.68 ± 0.01	–	–	DECam
20170128	57782.1	105.4	–	–	21.74 ± 0.02	21.58 ± 0.02	DECam
20170130	57784.1	107.3	22.27 ± 0.03	21.59 ± 0.02	–	–	DECam
20170204	57789.1	112.0	–	–	21.73 ± 0.05	21.54 ± 0.02	DECam
20170206	57791.1	113.9	22.62 ± 0.19	21.53 ± 0.02	–	–	DECam
20170215	57800.1	122.3	22.09 ± 0.03	21.58 ± 0.02	–	–	DECam
20170218	57803.5	125.5	–	–	21.39 ± 0.01	–	DECam
20170227	57811.5	133.1	–	21.55 ± 0.20	–	–	EFOSC2
20170325	57837.5	157.6	21.94 ± 0.10	21.48 ± 0.10	21.48 ± 0.10	–	EFOSC2
20170402	57845.5	165.1	–	21.00 ± 0.22	–	–	EFOSC2
20170412	57855.5	174.5	> 20.47	> 20.85	> 20.52	> 20.68	GROND
20170531	57905.4	221.5	–	21.60 ± 0.00	–	–	EFOSC2
20170601	57906.4	222.5	–	21.60 ± 0.00	–	–	EFOSC2
20170603	57908.4	224.3	–	21.73 ± 0.10	21.41 ± 0.00	–	EFOSC2
20170720	57955.9	269.1	–	23.04 ± 0.10	22.88 ± 0.06	–	LDSS3
20170727	57962.4	275.2	22.93 ± 0.05	22.65 ± 0.05	22.90 ± 0.11	23.19 ± 0.10	FORS2
20170821	57987.3	298.6	24.87 ± 0.27	23.39 ± 0.06	23.76 ± 0.10	23.36 ± 0.09	DECam
20170826	57992.3	303.4	24.80 ± 0.23	23.51 ± 0.06	23.81 ± 0.11	23.33 ± 0.12	DECam

UT date	MJD	Rest-frame phase (days)	g (mag)	r (mag)	i (mag)	z (mag)	Instrument
20170831	57997.3	308.1	–	–	23.76 ± 0.31	–	DECam
20170901	57998.2	308.9	–	–	23.53 ± 0.24	23.11 ± 0.24	DECam
20170902	57999.3	309.9	–	23.49 ± 0.13	–	23.47 ± 0.19	DECam
20170906	58003.3	313.7	–	23.44 ± 0.17	23.95 ± 0.19	23.37 ± 0.08	DECam
20170910	58007.4	317.6	–	23.51 ± 0.09	23.63 ± 0.12	–	DECam
20170912	58009.4	319.5	–	–	23.68 ± 0.12	23.35 ± 0.06	DECam
20170917	58014.2	324.0	24.68 ± 0.20	23.50 ± 0.05	–	–	DECam
20170923	58020.3	329.7	24.88 ± 0.28	23.64 ± 0.08	24.06 ± 0.10	23.33 ± 0.06	DECam
20171001	58028.2	337.2	–	23.52 ± 0.11	–	23.37 ± 0.09	DECam
20171009	58036.3	344.8	–	23.26 ± 0.11	23.93 ± 0.12	23.48 ± 0.09	DECam
20171013	58040.3	348.6	–	23.74 ± 0.07	–	23.66 ± 0.10	DECam
20171018	58045.3	353.3	24.90 ± 0.25	23.74 ± 0.07	24.04 ± 0.12	23.64 ± 0.11	DECam
20171025	58052.1	359.7	25.00 ± 0.24	23.85 ± 0.10	24.00 ± 0.15	23.54 ± 0.10	DECam
20171030	58057.2	364.5	–	23.70 ± 0.09	24.03 ± 0.12	23.55 ± 0.08	DECam
20171106	58064.2	371.1	–	23.53 ± 0.12	24.19 ± 0.16	23.67 ± 0.11	DECam
20171113	58071.2	377.7	–	23.79 ± 0.06	23.93 ± 0.10	23.62 ± 0.09	DECam
20171118	58076.3	382.5	25.17 ± 0.32	23.93 ± 0.10	24.19 ± 0.18	–	DECam
20171121	58079.1	385.1	–	–	–	23.79 ± 0.12	DECam
20171124	58082.2	388.0	–	23.92 ± 0.08	24.34 ± 0.17	–	DECam
20171126	58084.3	390.0	25.02 ± 0.36	–	–	23.75 ± 0.11	DECam
20171204	58092.2	397.4	–	–	–	23.90 ± 0.15	DECam
20171210	58098.2	403.1	–	23.93 ± 0.10	24.33 ± 0.17	23.85 ± 0.14	DECam
20171213	58101.2	405.9	–	24.09 ± 0.10	24.49 ± 0.17	–	DECam
20171219	58107.2	411.6	–	24.05 ± 0.07	24.73 ± 0.16	23.96 ± 0.13	DECam
20171229	58117.1	420.9	–	23.97 ± 0.31	24.70 ± 0.32	24.01 ± 0.22	DECam
20180105	58124.1	427.5	–	24.34 ± 0.08	24.65 ± 0.14	24.05 ± 0.11	DECam
20180112	58131.1	434.1	–	24.47 ± 0.30	25.17 ± 0.33	24.11 ± 0.12	DECam
20180118	58137.1	439.7	–	24.55 ± 0.14	–	24.37 ± 0.24	DECam
20180122	58141.1	443.5	–	24.65 ± 0.28	–	–	DECam

Notes: The magnitudes have not been corrected for extinction. **DECam:** Dark Energy Camera at Blanco 4-m telescope; **EFOSC2:** ESO Faint Object Spectrograph and Camera at the 3.5-m ESO New Technology Telescope (NTT); **GROND:** Gamma-Ray Burst Optical/Near-Infrared Detector at the 2.2-m MPG telescope; **LDSS3:** Low Dispersion Survey Spectrograph at the Magellan Clay 6.5-m telescope; **FORS2**: FOcal Reducer/low dispersion Spectrograph 2 at the ESO Very Large Telescope (VLT).

**Table A2.** χ^2 for the power-law and exponential fits

SN	χ^2 Power-law (accretion power)	χ^2 Exponential (^{56}Co decay)
DES16C3cje	1.624	3.403
SN 1987A	10.125	2.308
SN 2005cs	0.963	0.052
SN 2009E	5.587	0.283

Table A3. Parameters of the best models presented in Figure 4.

| Model	Mass ($M_\odot$)	Radius ($R_\odot$)	Energy (Foe)	Ni mass ($M_\odot$)	$\dot{M}_0$ ($M_\odot\,s^{-1}$)	Reference (Colour)
RSG	15	830	0.11	0.095	...	Green line
RSG	15	830	0.11	0.095	0.5×10^{-8}	Blue line
BSG	40	100	1.0	0.085	...	Cyan line
BSG	40	100	1.0	0.080	0.4×10^{-8}	Black line

APPENDIX B: FIGURES
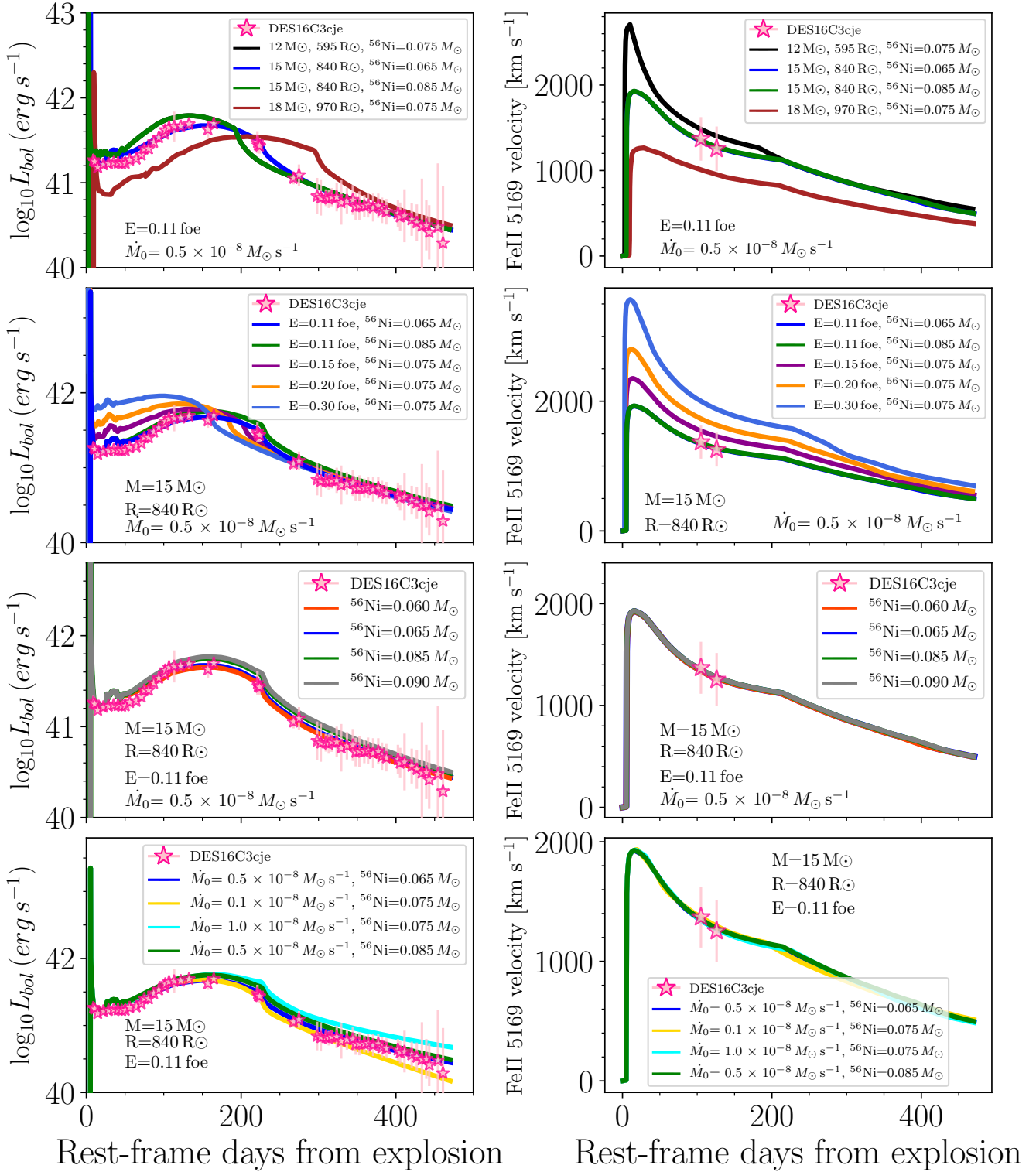
Figure B.1. Left: Bolometric light curve of DES16C3cje (stars) compared with the results of the light curve calculations from hydrodynamic models. For each plot, the legend shows the differences in the models, while the parameters with similar values are presented next to the curves. **Right:** Evolution of the photospheric velocity for the models presented in the left panel compared with measured Fe II 5169 Å line velocities of DES16C3cje.
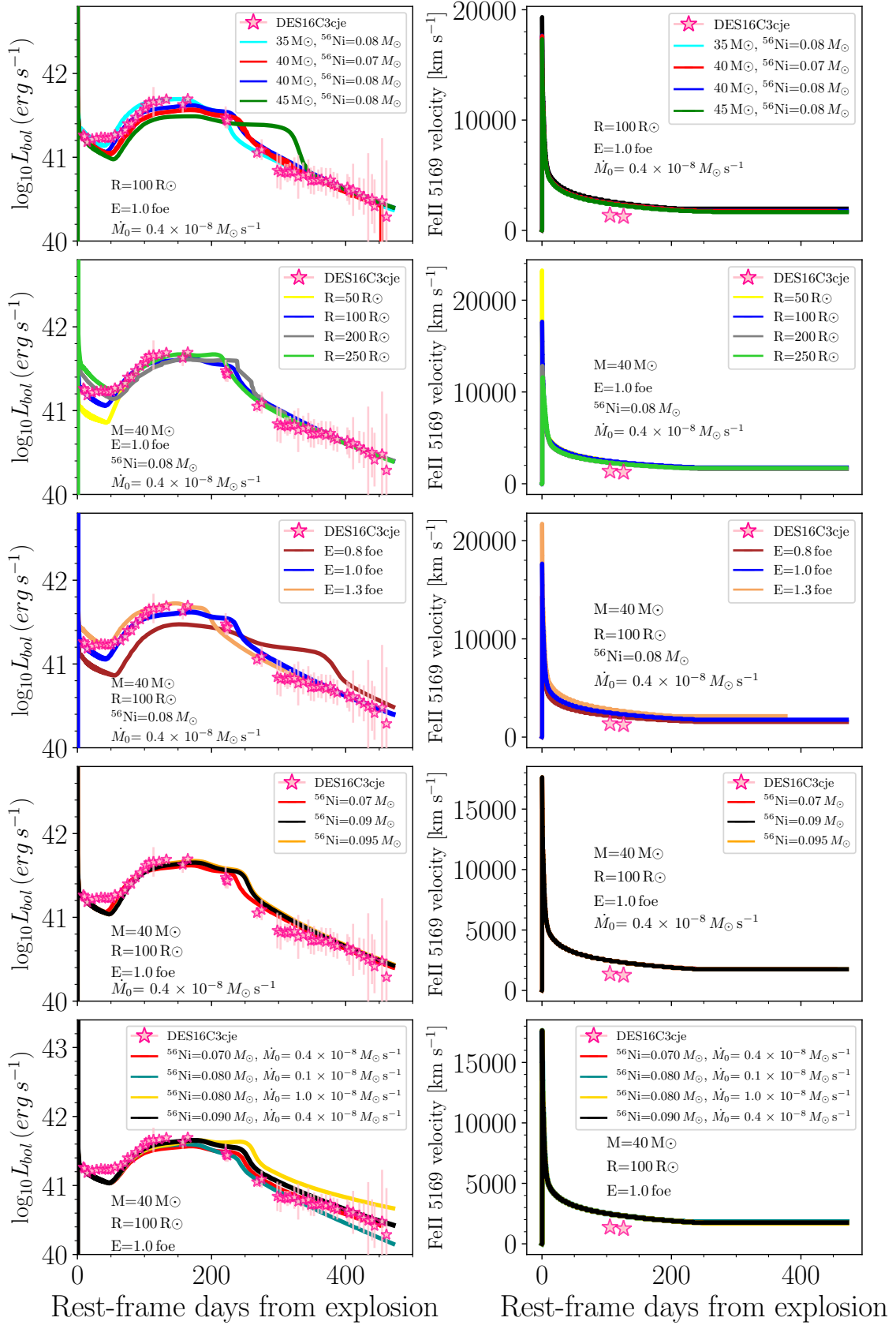
Figure B.2. Same as Figure B.1 but for more massive and relatively compact progenitors.

[1] Department of Physics and Astronomy, University of Southampton, Southampton, SO17 1BJ, UK

[2] Facultad de Ciencias Astronómicas y Geofísicas, Universidad Nacional de La Plata, Paseo del Bosque S/N, B1900FWA, La Plata,
Argentina

[3] Instituto de Astrofísica de La Plata (IALP), CCT-CONICET-UNLP. Paseo del Bosque S/N, B1900FWA, La Plata, Argentina

[4] Kavli Institute for the Physics and Mathematics of the Universe (WPI), The University of Tokyo, 5-1-5 Kashiwanoha, Kashiwa,
Chiba 277-8583, Japan

[5] School of Physics & Astronomy, Cardiff University, Queens Buildings, The Parade, Cardiff, CF24 3AA, UK

[6] European Southern Observatory, Alonso de Córdova 3107, Casilla 19, Santiago, Chile

[7] Division of Science, National Astronomical Observatory of Japan, 2-21-1 Osawa, Mitaka, Tokyo 181-8588, Japan

[8] INAF – Osservatorio Astronomico di Padova, Padova, Italy.

[9] Departamento de Física Teórica y del Cosmos, Universidad de Granada, E-18071 Granada, Spain

[10] Lawrence Berkeley National Laboratory, 1 Cyclotron Road, Berkeley, CA 94720, USA

[11] University of Copenhagen, Dark Cosmology Centre, Juliane Maries Vej 30, 2100 Copenhagen O, Denmark

[12] The Oskar Klein Centre, Department of Astronomy, Stockholm University, AlbaNova, 10691 Stockholm, Sweden.

[13] Max-Planck-Institut für Extraterrestrische Physik, Giessenbachstraße 1, 85748, Garching, Germany

[14] School of Mathematics and Physics, University of Queensland, Brisbane, QLD 4072, Australia

[15] Capodimonte Observatory, INAF-Naples , Salita Moiariello 16, 80131-Naples, Italy.

[16] European Southern Observatory, Karl-Schwarzschild-Str. 2, D-85748 Garching b. München, Germany.

[17] Santa Cruz Institute for Particle Physics, Santa Cruz, CA 95064, USA

[18] School of Physics, O'Brien Centre for Science North, University College Dublin, Dublin, Ireland.

[19] Institute of Cosmology and Gravitation, University of Portsmouth, Portsmouth, PO1 3FX, UK

[20] CENTRA, Instituto Superior Técnico, Universidade de Lisboa, Av. Rovisco Pais 1, 1049-001 Lisboa, Portugal

[21] Sydney Institute for Astronomy, School of Physics, A28, The University of Sydney, NSW 2006, Australia

[22] Astronomical Observatory, University of Warsaw, Al. Ujazdowskie 4, 00-478 Warszawa, Poland

[23] Tuorla Observatory, Department of Physics and Astronomy, University of Turku, FI-20014 Turku, Finland

[24] Observatories of the Carnegie Institution for Science, 813 Santa Barbara Street, Pasadena, CA 91101, USA

[25] School of Physics, Trinity College Dublin, The University of Dublin, Dublin 2, Ireland.

[26] Université Clermont Auvergne, CNRS/IN2P3, LPC, F-63000 Clermont-Ferrand, France

[27] Las Campanas Observatory, Carnegie Observatories, Casilla 601, La Serena, Chile

[28] Institute for Astronomy, University of Edinburgh, Royal Observatory, Blackford Hill, EH9 3HJ, UK

[29] Birmingham Institute for Gravitational Wave Astronomy and School of Physics and Astronomy, University of Birmingham, Birmingham B15 2TT, UK

[30] The Research School of Astronomy and Astrophysics, Australian National University, ACT 2601, Australia

[31] Departamento de Física Matemática, Instituto de Física, Universidade de São Paulo, CP 66318, São Paulo, SP, 05314-970, Brazil

[32] Laboratório Interinstitucional de e-Astronomia - LIneA, Rua Gal. José Cristino 77, Rio de Janeiro, RJ - 20921-400, Brazil

[33] Fermi National Accelerator Laboratory, P. O. Box 500, Batavia, IL 60510, USA

[34] Instituto de Fisica Teorica UAM/CSIC, Universidad Autonoma de Madrid, 28049 Madrid, Spain

[35] CNRS, UMR 7095, Institut d'Astrophysique de Paris, F-75014, Paris, France

[36] Sorbonne Universités, UPMC Univ Paris 06, UMR 7095, Institut d'Astrophysique de Paris, F-75014, Paris, France

[37] Department of Physics & Astronomy, University College London, Gower Street, London, WC1E 6BT, UK

[38] Kavli Institute for Particle Astrophysics & Cosmology, P. O. Box 2450, Stanford University, Stanford, CA 94305, USA

[39] SLAC National Accelerator Laboratory, Menlo Park, CA 94025, USA

[40] Centro de Investigaciones Energéticas, Medioambientales y Tecnológicas (CIEMAT), Madrid, Spain

[41] Department of Astronomy, University of Illinois at Urbana-Champaign, 1002 W. Green Street, Urbana, IL 61801, USA

[42] National Center for Supercomputing Applications, 1205 West Clark St., Urbana, IL 61801, USA

[43] Institut de Física d'Altes Energies (IFAE), The Barcelona Institute of Science and Technology, Campus UAB, 08193 Bellaterra (Barcelona) Spain

[44] INAF-Osservatorio Astronomico di Trieste, via G. B. Tiepolo 11, I-34143 Trieste, Italy

[45] Institute for Fundamental Physics of the Universe, Via Beirut 2, 34014 Trieste, Italy

[46] Observatório Nacional, Rua Gal. José Cristino 77, Rio de Janeiro, RJ - 20921-400, Brazil

[47] Department of Physics, IIT Hyderabad, Kandi, Telangana 502285, India

[48] Department of Astronomy/Steward Observatory, University of Arizona, 933 North Cherry Avenue, Tucson, AZ 85721-0065, USA

[49] Jet Propulsion Laboratory, California Institute of Technology, 4800 Oak Grove Dr., Pasadena, CA 91109, USA

[50] Institut d'Estudis Espacials de Catalunya (IEEC), 08034 Barcelona, Spain

[51] Institute of Space Sciences (ICE, CSIC), Campus UAB, Carrer de Can Magrans, s/n, 08193 Barcelona, Spain

[52] Kavli Institute for Cosmological Physics, University of Chicago, Chicago, IL 60637, USA

[53] Department of Astronomy, University of Michigan, Ann Arbor, MI 48109, USA

[54] Department of Physics, University of Michigan, Ann Arbor, MI 48109, USA

[55] Department of Physics, Stanford University, 382 Via Pueblo Mall, Stanford, CA 94305, USA

[56] Center for Cosmology and Astro-Particle Physics, The Ohio State University, Columbus, OH 43210, USA

[57] Department of Physics, The Ohio State University,

Columbus, OH 43210, USA

[58] Center for Astrophysics | Harvard & Smithsonian, 60 Garden Street, Cambridge, MA 02138, USA

[59] Australian Astronomical Optics, Macquarie University, North Ryde, NSW 2113, Australia

[60] Lowell Observatory, 1400 Mars Hill Rd, Flagstaff, AZ 86001, USA

[61] Department of Physics and Astronomy, University of Pennsylvania, Philadelphia, PA 19104, USA

[62] Institució Catalana de Recerca i Estudis Avançats, E-08010 Barcelona, Spain

[63] Department of Astrophysical Sciences, Princeton University, Peyton Hall, Princeton, NJ 08544, USA

[64] Brandeis University, Physics Department, 415 South Street, Waltham MA 02453

[65] Computer Science and Mathematics Division, Oak Ridge National Laboratory, Oak Ridge, TN 37831

[66] Universitäts-Sternwarte, Fakultät für Physik, Ludwig-Maximilians Universität München, Scheinerstr. 1, 81679 München, Germany

[67] Cerro Tololo Inter-American Observatory, National Optical Astronomy Observatory, Casilla 603, La Serena, Chile

[68] Department of Physics and Astronomy, Pevensey Building, University of Sussex, Brighton, BN1 9QH, UK

This paper has been typeset from a TeX/LaTeX file prepared by the author.